Open Research Online

Preservation of primordial signatures of water in highly-shocked ancient lunar rocks

Journal Item

© 2020 The Authors

Version: Version of Record

Link(s) to article on publisher's website:
http://dx.doi.org/doi:10.1016/j.epsl.2020.116364

oro.open.ac.uk

Preservation of primordial signatures of water in highly-shocked ancient lunar rocks

Ana Černok [a,b,c,*], Mahesh Anand [a,d], Xuchao Zhao [a], James R. Darling [e], Lee F. White [b,c], Alice Stephant [a], Joseph Dunlop [e], Kimberly T. Tait [b,c], Ian A. Franchi [a]

[a] *School of Physical Sciences, The Open University, Walton Hall, Milton Keynes, MK7 6AA, United Kingdom*
[b] *Centre for Applied Planetary Mineralogy, Department of Natural History, Royal Ontario Museum, Toronto, M5S 2C6, Canada*
[c] *Department of Earth Sciences, University of Toronto, Toronto, M5S 3B1, Canada*
[d] *Department of Earth Sciences, The Natural History Museum, London, SW7 5BD, United Kingdom*
[e] *University of Portsmouth, School of the Environment, Geography and Geosciences, Burnaby Road, Portsmouth, PO1 3QL, United Kingdom*

A B S T R A C T

Spurred by the discovery of water in lunar volcanic glasses about a decade ago, the accessory mineral apatite became the primary target to investigate the abundance and source of lunar water. This is due to its ability to contain significant amounts of OH in its structure, along with the widespread presence of apatite in lunar rocks. There is a general understanding that crustal cumulate rocks of the lunar magnesian (Mg) suite are better candidates for recording the original isotopic compositions of volatile elements in their parental melts compared to eruptive rocks, such as mare basalts. Consequently, water-bearing minerals in Mg-suite rocks are thought to be ideal candidates for discerning the primary hydrogen isotopic composition of water in the lunar interior. Mg-suite rocks and most other Apollo samples that were collected at the lunar surface display variable degrees of shock-deformation. In this study, we have investigated seven Apollo 17 Mg-suite samples that include troctolite, gabbro and norite lithologies, in order to understand if shock processes affected the water abundances and/or H isotopic composition of apatite. The measured water contents in apatite grains range from 31 to 964 ppm, with associated δD values varying between $-535 \pm 134‰$ and $+147 \pm 194‰$ (2σ). Considering the full dataset, there appears to be no correlation between H_2O and δD of apatite and the level of shock each apatite grain has experienced. However, the lowest δD was recorded by individual, water-poor ($<\sim 100$ ppm H_2O) apatite grains that are either directly in contact with an impact melt or in its proximity. Therefore, the low-δD signature of apatite could be a result of interactions with D-poor regolith (solar wind derived H), facilitated by shock-induced nanostructures that could have provided pathways for migration of volatiles. In contrast, in relatively water-rich apatites ($>\sim 100$ ppm H_2O), regardless of the complexity of the shock-induced nanostructures, there appears to be no evidence of water-loss or alteration in their δD. The weighted average δD value of 24 such water-rich apatites is $-192 \pm 71‰$, and, of all 36 analyzed spots is $-209 \pm 47‰$, indistinguishable from that of other KREEPy lunar lithologies or the Earth's deep mantle. Despite experiencing variable degrees of shock-deformation at a later stage in lunar history, water-rich apatite in some of the earliest-formed lunar crustal material appears to retain the original isotopic signature of H in the Moon.

1. Introduction

The phosphate mineral apatite $[Ca_5(PO_4)_3(F,Cl,OH)]$ is one of the most versatile minerals found in various rocks and meteorites (Hughes, 2015). As an abundant phosphate in extra-terrestrial sam-

ples, it has been used to assess their water budget (e.g., McCubbin and Jones, 2015), absolute ages (Göpel et al., 1994), and as a proxy for their oxidation conditions (Konecke et al., 2017). Apatite became the primary target to investigate the abundance and source(s) of the lunar water (McCubbin et al., 2010) soon after the discovery of water in lunar volcanic glasses (Saal et al., 2008). The past decade has witnessed many studies focusing on Secondary Ion Mass Spectrometry (SIMS and NanoSIMS) measurements of hydrogen abundances (expressed as either OH or H_2O)

* Corresponding author at: Department of Earth Sciences, University of Toronto, Toronto, M5S 3B1, Canada.
E-mail addresses: acernok@rom.on.ca, ana.cernok@gmail.com (A. Černok).

and H isotopic composition of apatite from most representative lunar lithologies, including mare basalts and various highlands samples (Anand, 2014; Barnes et al., 2014, 2013; Boyce et al., 2014, 2010; Greenwood et al., 2011; McCubbin et al., 2010; Pernet-Fisher et al., 2014; Robinson et al., 2016; Robinson and Taylor, 2014; Saal et al., 2013; Tartèse et al., 2014a, 2014b, 2013; Treiman et al., 2016). Water was looked for, and confirmed, in other host phases, too, for example within anorthosite (Hui et al., 2017, 2013), surface regolith (Liu et al., 2012; Stephant and Robert, 2014), melt inclusions (Hauri et al., 2011; Chen et al., 2015; Ni et al., 2019, 2017; Singer et al., 2017) and volcanic glasses (Füri et al., 2014; Saal et al., 2013). Altogether, these findings necessitated a re-evaluation of the "bone-dry" Moon paradigm, established in the early 1970s, heralding a new era in our quest for understanding the history of water in the lunar interior.

Water in apatite has been thoroughly investigated in most types of lunar basalts ranging from high-Ti and low-Ti basalts (e.g. Tartèse et al., 2013) to high-Al and KREEP-rich varieties, where KREEP stands for potassium (K), the rare earth elements (REEs), and phosphorus (P) (e.g., Greenwood et al., 2011; Tartèse et al., 2014b; Treiman et al., 2016). However, apatite in most mare basaltic samples crystallized at a late stage (>95% crystallization), by which time their parental melts were likely to have undergone significant H_2-degassing during ascent and upon eruption. This degassing could have induced isotopic fractionation of hydrogen (H) from deuterium (D) (e.g., Tartèse et al., 2013). The primary lunar crust, formed directly through Lunar Magma Ocean (LMO) solidification, is predominantly composed of anorthosites that do not contain apatite. Subsequently, incompatible-element-rich and Mg-rich magmas were emplaced into the overlying anorthositic lunar crust as deep crustal cumulates giving rise to Mg-suite rocks (summarized in Shearer et al., 2015). These rocks are thought to have better preserved the H isotopic composition of their parent melts (Barnes et al., 2016, 2014). Thus, the Mg-suite rocks are ideal targets for ascertaining the H isotopic composition of indigenous lunar water. We remain cognisant of the fact that some models suggest an impact origin for at least a portion of Mg-suite rocks (Shearer et al., 2015 and references therein), most recently for the troctolite 76535 (White et al., 2020). Altogether, the impact models suggest the cumulates could have crystallized in insulated, slow-cooling large melt sheets or pooled beneath the anorthositic crust (summarized in Shearer et al., 2015). However, no research has yet been carried out to investigate the effect of the large-scale impact melting on indigenous lunar volatile signature, such as might be the case for Mg-suite rocks, if they indeed crystallized from large melt sheets.

Regardless of their petrogenetic mode of formation, another important aspect of Mg-suite samples is that they have experienced certain levels of shock deformation after their initial crystallization. Experimental studies at elevated temperatures have shown H diffusion in apatite to be much faster than for all other elements, including Pb (Higashi et al., 2017), which would be relevant for apatite exposed to shock metamorphism. Apart from investigation of water in variably shocked anorthosite (Hui et al., 2017), this important aspect of lunar samples' history remains underexplored. To our knowledge, no similar efforts to understand the effect of shock deformation on volatiles in lunar samples have yet been undertaken, even though a clear need for this approach has been advocated (McCubbin et al., 2015). This is reinforced by observations of impact-associated volatile mobility within martian (Howarth et al., 2015) and terrestrial (Kenny et al., 2020) apatite.

Prior to this study, apatite water contents and H-isotopic compositions have only been investigated in three samples of Mg-suite lithologies (Barnes et al., 2014). These authors report water contents from <100 ppm to ~2000 ppm, associated with mostly terrestrial-like H isotopic composition. Based on this study, early-formed crustal rocks on the Moon were interpreted to contain water that shares a common origin with water on Earth. The potential sources of this water are further narrowed down to various types of chondritic materials. The most likely candidates are CM and CI-type carbonaceous chondrites, as they provide the closest fit to the Moon's bulk H and N compositions (Alexander et al., 2012; Alexander, 2017; Hallis, 2017, and references therein). Other constraints require that a significant proportion of the CI/CM material must have been accreted to Earth prior to the Moon-forming impact (Greenwood et al., 2018).

To investigate the influence of shock-induced deformation, metamorphism and impact-melting on apatite water abundance and H isotopic composition, we conducted a study on a suite of variably shocked rock-fragments and impact-melt breccias from the Apollo 17 collection. The texture, microstructure and petrological context of apatite is a critical parameter in understanding the severity of shock deformation and were characterized by detailed scanning electron microscope (SEM) imaging and electron backscatter diffraction (EBSD) analysis of each grain prior to measuring its water abundance and D/H ratio using a NanoSIMS.

2. Sample selection

The criteria for sample selection included geochemical pristinity, paucity of data on volatiles in Mg-suite apatites, and a sample set covering a range in level of shock deformation. The pristinity level of the samples (Warren, 1993) was taken into account with the aim of measuring the water content incorporated into the apatite lattice during its crystallization. All the selected samples have been previously characterized as compositionally pristine (Warren, 1993), meaning their bulk compositions and, in particular, highly siderophile elements (HSE) contents are representative of individual, unmixed, endogenous igneous rocks. At the same time, however, we targeted lithologies exposed to different levels of shock metamorphism.

Seven different lunar samples (nine specific thin-sections) of Mg-suite norite, troctolite and gabbro from the Apollo 17 collection were selected for this study. We previously determined the shock stage of some of the samples based on plagioclase shock-barometry (Černok et al., 2019 and references therein) and the shock microstructures of individual apatite grains using EBSD. These samples include troctolite 76535,51 (shock stage 1, S1), anorthositic troctolite 76335,60 (S2), Civet Cat norite fragment from the 72255,100 impact-melt breccia (S3–4), and heavily shocked norites 78235,43 and 78236,22 (S5 and S6). It is worth noting that the cooling history of the accessory mineral baddeleyite within the troctolite 76535 has recently been interpreted in the context of a large impact-melt sheet (White et al., 2020), despite not showing any compositional evidence for projectile contamination (Warren, 1993). The troctolite, however, does not display any shock features formed and has thus been assigned the deformation stage S1.

By applying the same criteria as in Černok et al. (2019) we here assess shock-stage deformation of apatite in troctolite 73235,136, as well as in three sections containing different lithologies inside an impact-melt breccia 76255 (norite 76255,68; gabbro 76255,71 and troctolite 76255,71). EBSD data acquired from these apatites can be found in Supplementary Material (SM, Supplementary Fig. 1). A list of studied samples, their cosmic ray exposure (CRE) ages, and all analyzed apatite grains with their interpreted shock-deformation stages is provided in Table 1. Thus, the selection of samples covers all representative lunar Mg-suite lithologies and shock histories, including coherent rock specimens, lithic fragments included within polymict impact breccia, and impact-melt matrix. Detailed sample descriptions, including associated
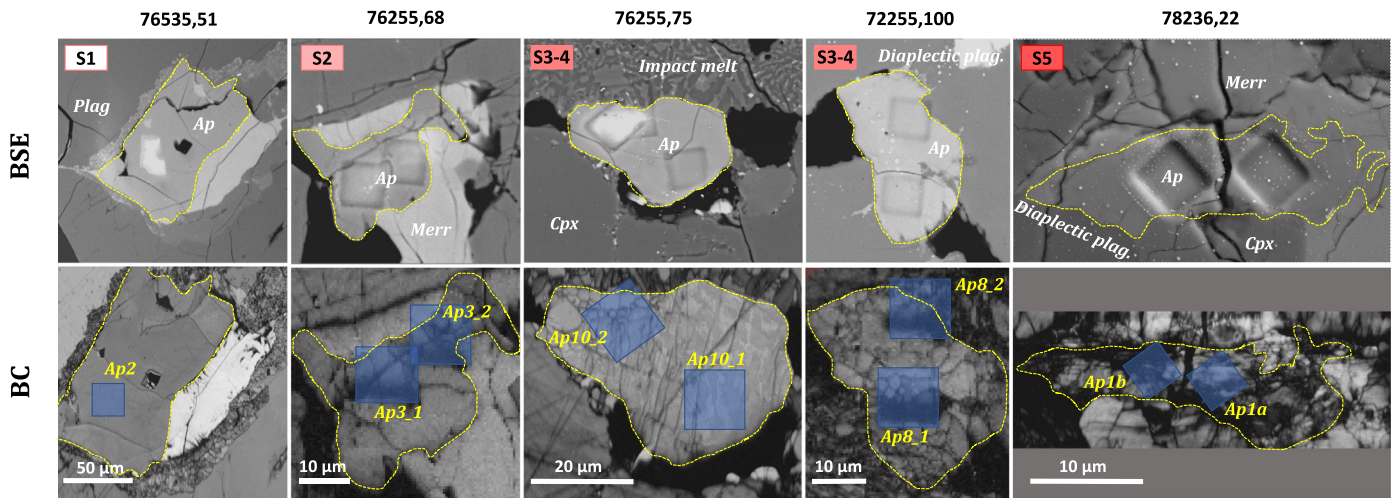
Fig. 1. Backscattered electron (BSE) and EBSD band contrast (BC) images of selected primary apatite grains, highlighted by yellow dashed line. Apatite is shock-deformed at variable conditions and the shock stage (S1–S5) is annotated in each case. Apatite at S6 did not show any diffraction (Černok et al., 2019). NanoSIMS analytical spots (pits) are visible in BSE images and their positions are marked by squares on BC images. Samples 76535, 72255 and 78236 were investigated earlier (Černok et al., 2019). EBSD data for other primary apatite grains is included in Supplementary Fig. 1. (For viewing the figure(s) in color, the reader is referred to the web version of this article.)

geochronological information, are provided in Supplementary Material.

3. Analytical techniques

Polished thin-sections of Apollo samples were used in this study. All sections were prepared at NASA Johnson Space Center using a water-free medium, and mounted onto a glass slide using araldite epoxy (see Tartèse et al., 2013 for further details).

3.1. Scanning Electron Microscopy and Electron Backscatter Diffraction (EBSD)

The studied polished thin-sections were carbon-coated and examined using a Quanta 3D Focused Ion Beam Scanning Electron Microscope (FIB-SEM) at The Open University, equipped with an Oxford Instruments INCA energy dispersive X-ray detector. The electron beam was generated with an acceleration voltage of 15–20 kV and a current of 0.52 to 0.62 nA. A working distance of 15 mm was used for the generation of secondary electron (SE) and backscatter electron (BSE) images, as well for the acquisition of energy dispersive spectra (EDS). Micro- to nano-scale structural analysis was conducted by EBSD using an Oxford Instruments Nordlys EBSD detector mounted on a Zeiss EVO MA10 LaB$_6$-SEM housed at the University of Portsmouth (see SM and Supplementary Table 1), following earlier protocols (Darling et al., 2016; Černok et al., 2019).

3.2. H measurements using NanoSIMS

Following EBSD analyses, apatites were selected based on their textural context and microstructural features for *in-situ* measurements of H content (expressed as equivalent H$_2$O) and associated H isotopic composition (expressed using δD notation). We used a CAMECA NanoSIMS 50L at The Open University, following the protocol reported by Barnes et al. (2013) and applied in several subsequent studies (Barnes et al., 2014; Barrett et al., 2016; Tartèse et al., 2013). Thin-sections of the samples were covered by a 20–30 nm thick layer of carbon coat, kept for approximately one week in a vacuum oven at 40 °C, and then placed into the instrument airlock under the vacuum of $\sim 8 \times 10^{-8}$ Torr or better for 2–3 days before the start of each analytical session. An indium block containing the apatite standards Ap003, Ap004 and Ap018 (McCubbin

et al., 2012) and the nominally anhydrous San Carlos (SC) olivine, were simultaneously carbon coated with the samples and kept in the vacuum along with the samples. The apatite standards and the SC olivine are used for calibration and background corrections, respectively. Details on instrumental parameters, data reduction, analytical background and spallation corrections are provided in the SM, Supplementary Table 2, and Supplementary Figure 2.

3.3. Electron Probe Microanalysis

Electron probe microanalysis (EPMA) was performed on all apatite grains after analysis by NanoSIMS, to avoid any volatile loss by exposure to intense electron beam of the EPMA. Analyses were undertaken using the CAMECA SX100 instrument at The Open University, with protocols that were slightly modified after previous studies (e.g., Barnes et al., 2013; Tartèse et al., 2013). Analytical conditions are documented in SM and in Supplementary Table 4.

4. Results

4.1. Textural context and shock-induced microtexture of apatite

In the studied selection of coherent rock fragments and impact-melt breccias, we observed two distinct types of apatite based on their nanostructure. The *primary* apatites show variable degrees of internal nanostructural complexities induced by shock-induced deformation, ranging from stage S1 to S6 (Fig. 1). They were found in all coherent rocks and within lithic clasts inside the breccia, in contact with another primary, magmatic mineral assemblage (Fig. 1). The *secondary* apatites show no nanostructural complexities and were exclusively associated with impact melt in the matrix of all three 76255 breccia samples (Fig. 2).

Primary apatite is less abundant (a few grains per thin section) and is comparably small, with the largest grains reaching up to ~50 to 100 μm in their longest dimension. The microtexture and nanostructure of apatite from samples 76535, 76335, 72255, 78235 and 78236 were reported in a previous study (Černok et al., 2019). Following the criteria used in Černok et al. (2019), we assess the extent of shock-deformation stages in all other primary apatite grains in samples 76255 and 73235 based upon nanostructural data presented in Supplementary Fig. 1. In brief, the criteria used include the extent of subgrain size (defined by shape
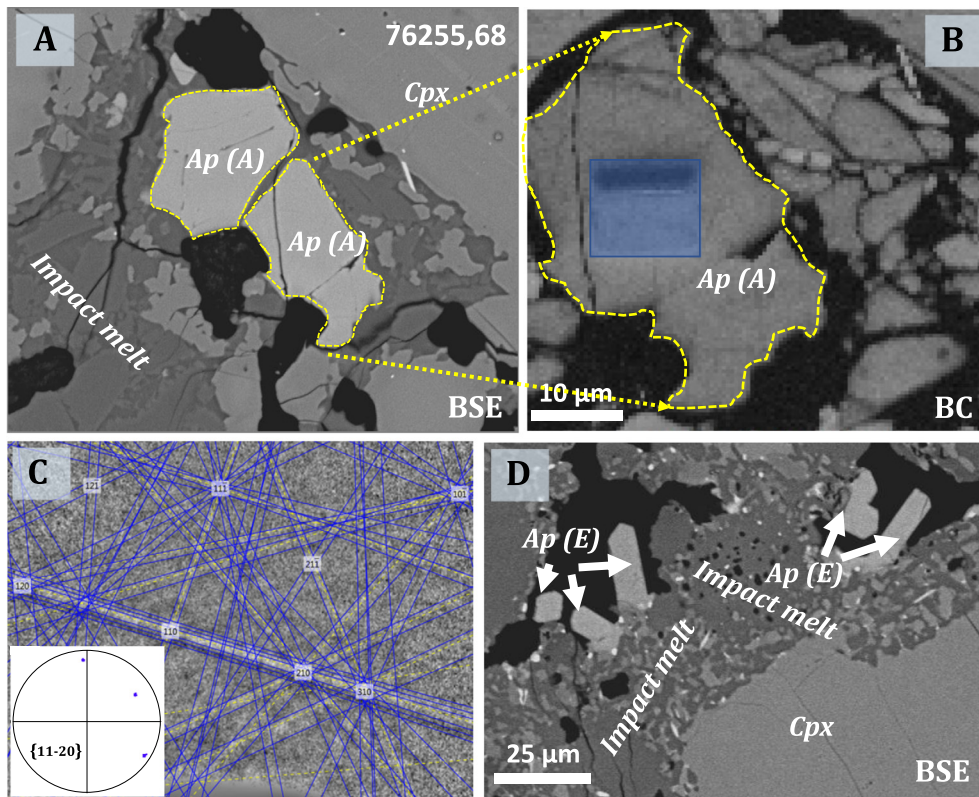
Fig. 2. BSE and BC images of selected secondary apatite grains in sample 78255,68, in contact with impact melt. A) BSE image of anhedral apatite grain (annotated A) surrounded by impact melt and voids. B) Band contrast image of the part of the grain presented in A revealing undisturbed interior. C) Electron backscatter pattern (EBSP) collected on the grain in A and B, and the derived pole figure. D) Euhedral secondary apatite (annotated E) growing inside voids of the impact melt.

or low angle grain boundaries of $<20°$), their density and total misorientation across the grain surface, which is a useful measure of crystal-plastic deformation (CPD). The observed features were derived from band contrast (BC) images, texture component (TC) maps and associated pole figures (Supplementary Fig. 1). We previously established that the internal nanostructure of primary apatite shows progressively higher levels of deformation with increasing shock level, ranging from no discernible nanostructural complexities at S1, to the maximum observed CPD at S5 as recorded by $\sim25°$ of total misorientation across apatite grains (Černok et al., 2019). Apatite within lithic fragments in all 76255 sections typically contain large subgrains and low degrees of CPD, which is comparable to apatite from S2 stage of deformation (Černok et al., 2019). More complex subgrain formation, along with 15–20° of total misorientation, was observed in apatite from troctolite 73235,136 and one apatite grain in 76255,71 (Ap10, Fig. 1 and Supplementary Fig. 1) that occurs at the contact of a large pyroxene clast and the fine-grained impact melt. These features are comparable to apatite from S3–S4 stages of shock deformation (Černok et al., 2019).

All secondary apatites were found in sample 76255, in impact-melt portions of all three thin sections (68, 71 and 75). This textural type is very abundant (several dozen per thin section) and forms, on average, larger grains that reach up to ~200 μm in the longest dimension. Most secondary apatites appear to be individual, anhedral (A) mineral grains within an impact melt with scalloped grain outlines (Fig. 2A and B), but a few euhedral (E) crystals were also observed (Fig. 2D). All secondary apatites, regardless of their shape, show strong diffraction patterns with unique orientation throughout the interior that are easily indexed with a good fit to the predefined apatite structure. They yield band contrast images (Fig. 2B) and inverse pole figures representative of single, undeformed crystals (Fig. 2C). They demonstrate a lack of sub-grain

formation or any other evidence of internal structural complexities (Fig. 2B, C). The anhedral grains, with scalloped outlines, are possibly xenocrysts that recrystallized in contact with the impact melt (Fig. 2A, B). However, considering the sub-euhedral to anhedral shape of fine-grained plagioclase and pyroxene from the impact melt in contact with this apatite (Fig. 2A, B, D), we cannot exclude a possibility that these anhedral grains crystallized directly from the melt. The euhedral apatite unambiguously grew directly from the impact melt (Fig. 2D). In summary, NanoSIMS analyses were performed on twenty-eight individual apatite grains previously characterized by EBSD. Eighteen apatite grains are of primary origin (S1–S6) while another ten are secondary in origin, of either anhedral (A) or euhedral (E) shape.

4.2. Composition of Mg-suite apatite

The measured composition of Mg-suite apatite studied here (Fig. 3) is comparable to that of previously reported data from highlands apatites (e.g. Barnes et al., 2014; McCubbin et al., 2015). All grains are fluorapatite (F > Cl > OH), most of which have Cl-content varying from 0.5 to 1.2 wt%. Apatites in troctolites 76535 and 76335, as well as in the norites 78236 and 72255 show the highest Cl abundance (>0.8 wt%). All studied grains within breccia 76255 contain ~0.6 wt% Cl, except for the Ap3 in 76255,75 which contains only 0.2 wt% Cl. Similarly, the sole apatite grain in 73235 troctolite contains 0.2 wt% Cl. Due to unreliable F-measurement using EPMA protocol without TDI-correction, the F-content (Fig. 3) was calculated by subtracting OH content, determined by NanoSIMS, and Cl content, determined by EPMA (see Supplementary Table 5 for exact composition and stoichiometry). The obtained difference between the estimated and measured F content do not show significant discrepancies for most of the studied grains (Supplementary Table 5). The most common impu-
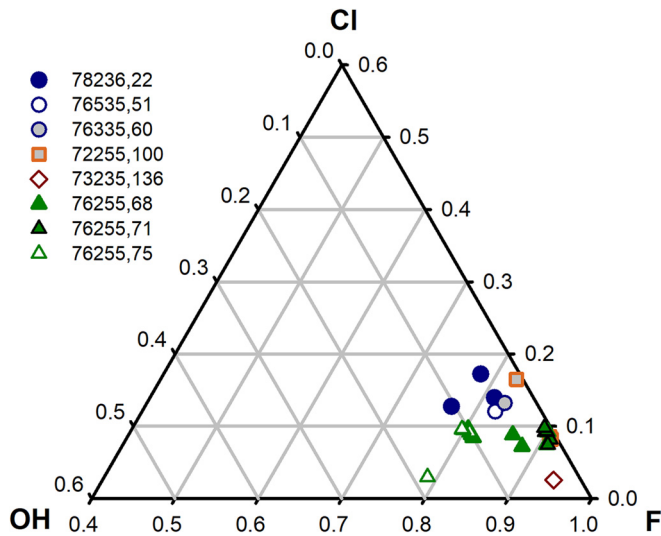
Fig. 3. EPMA composition of studied apatites. All apatites are F-apatites with Cl-content varying from 0.2–1.2 wt% and OH-content varying up to 960 ppm (see Supplementary Table 5 for exact composition and stoichiometry). Stoichiometry calculation based on 26 anions formula $Ca_{10}(PO_4)_6(F, Cl, OH)_2$.

rities in all studied apatites are Fe, Mg, and Si. The Cl-rich apatites (troctolites 76535 and 76335; norites 78235 and 78236) contain a negligible amount of Ce, Nd, and Y compared with the Cl-poor apatite in impact melt breccia 76255, Civet Cat norite 72255, and troctolite 73235. No obvious difference in major element composition is observed between primary and secondary apatite in the breccia 76255.

4.3. H_2O abundance and δD composition

Apatite in shocked Apollo 17 rocks shows a wide range in water concentrations and in δD values (Table 1 and Fig. 4). As a number of apatite grains contain low water abundance (i.e., <100 ppm H_2O), consideration must be given to spallogenic D and H that significantly contribute towards the measured H abundance, and more drastically, to D/H isotopic ratios (e.g., Füri et al., 2017; Saal et al., 2013). We report spallation corrected data using both available D-production rates (Table 1, Fig. 4, Supplementary Table 3, and Supplementary Figure 3; Füri et al., 2017; Merlivat et al., 1976), considering CRE ages listed in Table 1. However, for the remainder of the discussion, we use δD values corrected after Merlivat et al. (1976), as we find it better suited for the apatite analyses (see further discussion on Spallation corrections in SM).

The total range of water content measured in Mg-suite apatites varies between 31 ppm and 964 ppm, with δD values ranging from $-535 \pm 134\permil$ to $+147 \pm 194\permil$ (all uncertainties reported at the 2σ confidence level). The error-weighted average δD value for all 36 analyzed spots, including water-poor (<100 ppm H_2O) and water-rich (>100 ppm H_2O) is $-209 \pm 47\permil$. The weighted average δD value of 24 individual analyses that exclude water-poor (<100 ppm H_2O) apatite is indistinguishable within uncertainty ($-192 \pm 71\permil$). Thus, we refer to the weighted average value derived by all 36 spots in further discussions when referring to the entire dataset. Unshocked troctolite 76535,51 has 53 ± 1 ppm H_2O and δD of $-419 \pm 201\permil$. Cataclastic troctolite 76335 shows a range in H_2O content from 166 to 471 ppm. As no CRE ages are reported for this sample, we have applied spallogenic correction based on the conservative estimate for the CRE age of 76535 troctolite (233 ± 16 million years), because the two samples could be related (see sample description in SM). The cataclastic troctolite shows δD variations from $-350 \pm 123\permil$ to $-81 \pm 110\permil$, with a weighted average of $-193 \pm 83\permil$. Apatite within impact

melt breccia 76255 sections (76255, 68; 76255,71 and 76255,75) contain between 36 ppm and 964 ppm H_2O, with δD values varying from $-475 \pm 144\permil$ to $-59 \pm 175\permil$. Weighted average δD value of 20 apatites from all three sections is $-218 \pm 45\permil$, with that of 10 secondary apatites being indistinguishable from it ($-217 \pm 44\permil$). Across the individual sections, grains in the troctolite-bearing (76255,75) clast have the highest water content of all analyzed apatites (533–964 ppm) but show similar δD values ($-177 \pm 45\permil$). The section with noritic clasts in impact melt (76255,68) contain less than $\sim$270 ppm H_2O, with an exception of an individual spot (Ap10) that has $\sim$500 ppm water, and a weighted δD value of $-248 \pm 84\permil$. Apatite in the section containing the gabbro clast (76255,71) has among the lowest water contents, with less than 90 ppm H_2O, apart from one individual spot (Ap10, 679 ppm) and an associated δD value $-230 \pm 77\permil$ that is comparable to other samples. In summary, in the breccia 76255 no obvious difference in water content or the associated δD is observed between clast-hosted (primary) and melt-hosted (secondary, i.e., either recrystallized or grown from impact melt) apatites. Two apatites in norite clast Civet Cat have 31–62 ppm H_2O and show highly variable δD values ranging from $-535 \pm 134\permil$ up to $-124 \pm 173\permil$. Highly shocked norites 73235,43 and 78236,22 host apatite that contains 175 ppm to 634 ppm H_2O, with δD values ranging from $-288 \pm 128\permil$ to $136 \pm 171\permil$, resulting in a weighted average δD value of $-81 \pm 172\permil$.

Due to the fact that three different studies, including this one, have shown large discrepancies in δD values of the water-poor troctolite 76535 with old CRE ages (Robinson et al., 2016; Barnes et al., 2014), we exclude this sample from any further discussions on interpreting the volatiles data on lunar crustal samples and consider it as an 'anomalous' sample in this context (see further discussion in SM). However, a good internal consistency of D/H measured in control sample 78235 (Barnes et al., 2014) provides confidence in the reproducibility of our results.

5. Discussion

5.1. H_2O and δD of Mg-suite apatite in the context of its nanostructure and shock-deformation

The measured water contents are well within the range of values previously reported for apatite in different highlands lithologies (Fig. 5), including evolved rocks such as felsite, quartz-monzodiorites, and granite clasts in breccias, but also the Mg- and alkali-suite samples (Greenwood et al., 2011; Barnes et al., 2014; Robinson et al., 2016). Similar abundances were measured in apatite from KREEP and high-Al basalts (Greenwood et al., 2011; Tartèse et al., 2014a,b). The water-rich apatites measured here contain water in abundances also comparable to that of the lower-end values reported for apatite in low-Ti and high-Ti basalts (Fig. 5; Barnes et al., 2013; Tartèse et al., 2013, 2014a; Pernet-Fisher et al., 2014; Treiman et al., 2016). Our measurements do not show any particular lithology-specific variabilities in water abundances, as recorded in apatite, but do show that not all troctolite-hosted apatite grains are water-poor, as previously inferred (e.g., Barnes et al., 2014).

δD values of the Mg-suite apatite, ranging from $-535 \pm 56\permil$ to $+147 \pm 224\permil$ (2σ), reveal a pattern in which mostly the water-poor apatite (<100 ppm H_2O) are depleted in D relative to the water-rich apatite. This range of δD values is within that measured in carbonaceous chondrites ($-587\permil$ to $+207\permil$, Alexander et al., 2012), with the most of the analyzed grains showing the δD values within the range reported for the Earth's mantle ($\sim -220\permil$ to $-60\permil$; Hallis et al., 2015; McCubbin and Barnes, 2019). The weighted average δD value ($-209 \pm 47\permil$, 2σ) is indistinguishable from that reported for the Earth's deep interior (e.g. Hallis et

Table 1
Sample description, H_2O content and δD values of all analyzed apatites.

Sample description					H_2O abundance and δD			
Sample	Pristinity	CRE	Shock stage	Analysis point	H_2O	2σ	δD	2σ
78235,43 and 76236,22	8	292 ± 14	S5	78235,43_ac_Ap3b_1	510	6	136	171
			S5	78235,43_ac_Ap4a_1	634	7	147	194
			S5	78236,22_ac_Ap1a_1	249	3	−140	140
			S5	78236,22_ac_Ap1b_1	554	6	−28	159
			S6	78236,22_ac_Ap2_1	174	2	−288	128
76335,60	pr	$233 \pm 16^*$	S2	76335,60_10Oct17_Ap1_1	203	3	−260	130
			S2	76335,60_10Oct17_Ap1_2	202	3	−206	119
			S2	76335,60_10Oct17_Ap3_1	166	2	−99	157
			S2	76335,60_10Oct17_Ap4_1	245	4	−159	119
			S2	76335,60_10Oct17_Ap5_1	471	7	−81	110
			S2	76335,60_10Oct17_Ap6_1	246	4	−350	123
76255,68	7	27 ± 3	A	76255,68_11Oct17_Ap1_1	269	4	−267	115
			S2	76255,68_12Oct17_Ap2_1	88	1	−168	145
			S2	76255,68_12Oct17_Ap3_1	108	2	−59	175
			S2	76255,68_21Oct17_Ap3_2	36	1	−475	144
			A	76255,68_11Oct17_Ap4_1	253	4	−372	106
			A	76255,68_11Oct17_Ap4_2	115	2	−226	125
			A	76255,68_12Oct17_Ap6_1	104	2	−225	136
			E	76255,68_12Oct17_Ap10a_1	197	3	−130	142
			E	76255,68_12Oct17_Ap10b_1	531	8	−208	89
76255,75	8	27 ± 3	S2	76255,75_23Oct17_Ap03_1	964	15	−172	85
			S2	76255,75_23Oct17_Ap03_2_1	825	13	−257	99
			A	76255,75_23Oct17_Ap06a	533	8	−174	91
			A	76255,75_23Oct17_Ap07a	570	9	−116	96
			A	76255,75_23Oct17_Ap08	564	9	−171	91
76255,71	7	27 ± 3	A	76255,71_24Oct17_Ap01	52	1	−214	160
			A	76255,71_24Oct17_Ap05	46	1	−400	150
			A	76255,71_24Oct17_Ap06	41	1	−229	179
			S2	76255,71_24Oct17_Ap08	88	1	−120	150
			S3-4	76255,71_24Oct17_Ap10_1	82	1	−283	164
			S3-4	76255,71_Ap10_2_2Jul18	679	7	−218	56
73235,136	pr	110 ± 10	S3-4	73235,136_25Oct17_Ap1	75	1	−169	224
76535,51	9	233 ± 16	S1	76535,51_Ap2_2Jul18	53	1	−419	201
72255,100	8	44 ± 3	S3-4	72255,100_13Oct17_Ap3_1	41	1	−535	134
			S3-4	72255,100_13Oct17_Ap8_1	31	1	−210	200
			S3-4	72255,100_13Oct17_Ap8_2	62	1	−124	173

Note: H_2O abundance and δD values are corrected for IMF, background and spallation contribution. D-production rate after Merlivat et al. (1976). S1–S6 stands for shock-stage of primary apatite, A – anhedral secondary apatite, E – euhedral secondary apatite. For more details see extended Supplementary Table 3. CRE age of 76335 has not been reported, thus we apply the CRE of the petrologically similar 76535 troctolite.
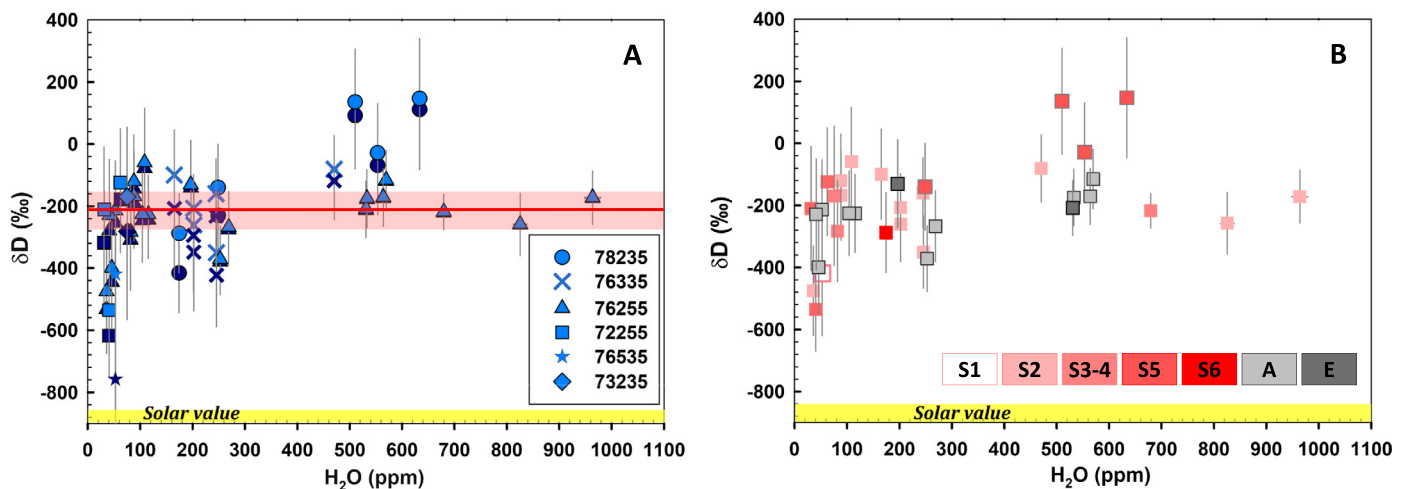
Fig. 4. H_2O-δD diagram of shocked apatite from a range of Mg-suite rocks. A) Light blue symbols represent spallation corrected δD values using cosmic ray D production from Merlivat et al. (1976) while dark blue symbols represent data corrected after Furi et al. (2017). The red line represents the weighted average δD value ($-209 \pm 47\permil$) of all analyzed spots. B) Different shock stages of primary (S1–S6), secondary anhedral (A) and secondary euhedral (E) apatite, using correction after Merlivat et al. (1976).
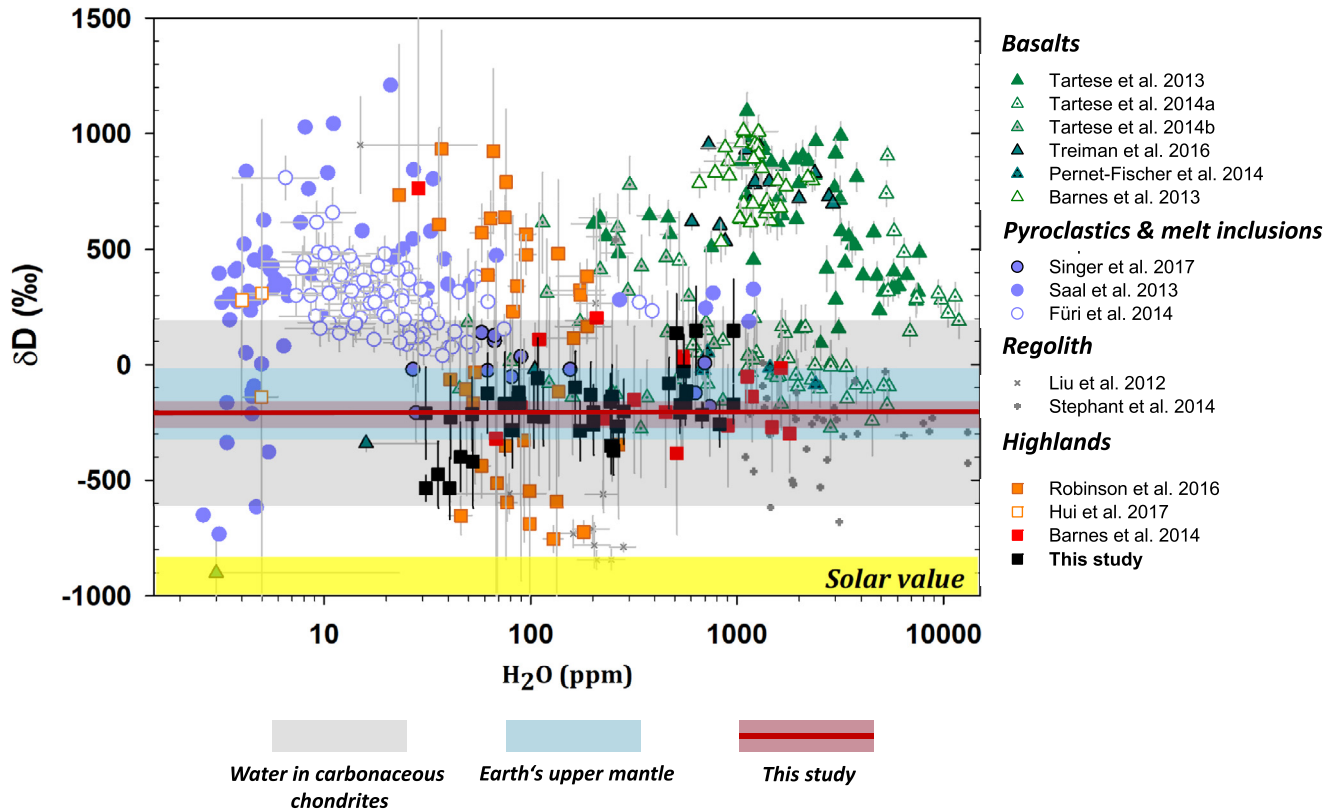
Fig. 5. δD values vs. H_2O contents from a wide range of lunar lithologies including pyroclastic lunar glasses, melt inclusions, regolith, anorthite and apatites. Reference values for Earth and carbonaceous chondrites are also provided (Hallis et al., 2017; Alexander et al., 2012; Alexander, 2017). Note the logarithmic scale of the H_2O axis. Error bars on Saal et al. (2013) data are omitted for clarity. The red line represents the weighted average δD value ($-209 \pm 47\permil$) of all apatite analyzed in this study.

al., 2015) and for the lunar KREEPy rocks (McCubbin and Barnes, 2019). The lowest δD signature is restricted to a handful of individual analyses in shocked *Civet Cat* norite 72255, impact-melt breccia 76255 and one spot in troctolite 76335 (Table 1, see section 5.3).

The overall H_2O-δD trend observed in this study does not seem to correlate with the level of shock deformation experienced by individual apatite grains (Fig. 4b). For instance, apatites in the two most heavily-deformed norites, 72255 *Civet Cat* and 78236, plot at the opposite ends of the observed H_2O-δD range. Results from impact-melt breccia 76255, which contains primary apatite inside lithic clasts (norite, gabbro and troctolite) and secondary apatite in the surrounding fine-grained impact melt, span across the entire H_2O-δD range seen in this study. However, apatites from each individual clast and the surrounding impact melt have distinct H_2O-δD values. For example, secondary apatite in 76255,68 contains similar amount of water as primary apatite inside the norite clast (Table 1), but in most cases the content is different than in the troctolite and the gabbro sections. This could indicate that the water abundance in the impact melt was not well homogenized or that the variable water abundances in the crystallizing apatite are being dictated by complex partitioning behavior of F, Cl and OH in the melt. Lithic clasts incorporated in the impact melt are shock-deformed at pressures and temperatures (S2) insufficient for their incipient melting, so the impact melt was not derived from those exact clasts. Instead, they were incorporated as coherent, unmelted clasts inside an already formed impact melt. However, the source rock must have had similar composition and contained apatites of comparable volatile signature. The source rock apatites that recrystallized in contact with impact melt, possibly acted as nuclei for further growth of secondary, anhedral apatite. Source apatite that melted in contact with impact melt was the main phosphorous and volatile source to form euhedral secondary apatite within the impact melt. Indistinguishable mineral chemistry of primary

and secondary apatite associated with indistinguishable δD values, despite their obvious textural and microstructural differences, further strengthens the hypothesis of similarity with the source rock. These results strongly suggest that no discernible water loss and no preferential loss of H over D is recorded in apatite as a result of the impact.

This result is surprising, taking into account very high H-diffusivity in apatite, which is expected to be even higher at temperatures relevant to impact melt (e.g. Higashi et al., 2017). Nevertheless, shock-experimental study on plagioclase (Minitti et al., 2008a) and *in situ* studies of Apollo highlands samples (Hui et al., 2017) have reported that this nominally anhydrous mineral behaves in a similar way to apatite, as observed in this study, despite an expected increase in H-diffusion at high temperatures (Johnson and Rossman, 2013). However, other minerals show very different behavior. For example, meteorite-relevant amphiboles (Minitti et al., 2008b, 2008a) experience slight water-enrichment, followed by an increase in δD when studied in the same shock-experiment as plagioclase. On the other hand, D-heavy signature of martian atmosphere is seen in numerous shock-affected minerals found in martian meteorites, implying that shock-induced textures can enhance mixing of different reservoirs. Furthermore, individual grains of martian phosphates have been observed to undergo devolatalization during an impact event (Howarth et al., 2015) or due to shock-induced phase transitions (Adcock et al., 2017). In contrast, ringwoodite, formed as a high-pressure polymorph of water-poor olivine in martian meteorite Tissint (Hallis et al., 2017), was observed to incorporate more water, aided by the shock-induced phase transition. This resulted in a considerably higher δD signature of ringwoodite, arising from incorporation of D-heavy martian atmosphere into the mineral.

In summary, the current understanding of shock-induced changes in volatile signatures is seemingly ambiguous, given that

both water-bearing and nominally anhydrous minerals have been observed to be affected but also entirely unaltered by shock-deformation processes. Based on this comprehensive study, reporting the largest dataset currently available, of water abundance and H isotopic composition from systematically analyzed shocked apatite in lunar samples, we conclude that relatively water-rich apatite in Mg-suite rocks are not affected by shock processes in terms of their water inventory and δD signatures – a finding that is likely to be of relevance to other shock-related apatite occurrences, particularly originating from airless bodies (e.g., 4Vesta).

5.2. Source of low-δD water

The lowest value δD of $-535 \pm 134‰$ is measured in Ap3 in 72255,100 (S3-4), followed by four other very low δD ($< -300 ‰$) grains: Ap5 in 76255,71 (A); Ap3 (S2), Ap4 (A) in 76255,68 and Ap6 (S2) in 76335,60. Samples 72255 and 76255 show relatively young CRE ages (44 ± 3 Ma and 27 ± 3 Ma, respectively), which result in negligible spallation correction (Supplementary Fig. 3). Therefore, these low-δD occurrences are to be considered as exceptional and not representative of the entire sample suite. The sole occurrence of low δD ($-350 \pm 123‰$) in 76335 should be viewed with caution, as no CRE age has been reported from this rock. Comparably low-δD values were reported for shocked quartz-monzodiorite samples 15403 and 15404 (Robinson et al., 2016), impact-melt breccia 15405 (Barnes et al., 2014), and for low-Ti basalt 12040 (Treiman et al., 2016).

Grains Ap3 and Ap4 in 76255 show a large intragranular inhomogeneity, with both grains showing spatially resolved, distinct δD values. Due to this fact, we exclude the possibility that our samples record a primitive low-δD reservoir, as inferred by previous studies (Robinson et al., 2016), and conclude that the source of low-δD must be of secondary origin. Direct implantation of solar hydrogen into apatite, found in these samples, is unlikely because solar wind can only penetrate < 1 μm under the surface of directly exposed grains (e.g., Robinson et al., 2016). The main low-δD (i.e., H-rich) reservoir on the Moon is the surface regolith (e.g., Liu et al., 2012; Treiman et al., 2016), containing fine grains with long exposure to surface implantation of solar-wind hydrogen. Treiman et al. (2016) suggested that the D-poor signature of apatite they measured in basalts, reflects mixing with a regolith component. The physical mechanism for introduction of hydrogen into apatite is likely to be thermal degassing of the D-poor regolith, induced by the heat of a nearby impact or, in case of mare basalts, the heat of basalts themselves (Treiman et al., 2016 and references therein). Similar regolith-interaction processes were recognized in high-Al basalt 14053 (Greenwood et al., 2011; Taylor et al., 2004) and olivine-hosted melt inclusions in basalts (Singer et al., 2017). Traces of trapped solar noble gasses within the sample 76255 were reported early on (Bogard et al., 1975, and references therein), however, they seem to be absent in 72255 breccia (Leich et al., 1975).

In addition, impact-melt breccia 15405 was reported to contain apatite with variable δD composition (Barnes et al., 2014). Robinson et al. (2016) excluded regolith as a source of D-poor water following a different line of arguments; they calculated that even the maximum amount of regolith which could have been assimilated by the impact melt, produced by the formation of Aristillus crater, the possible source of the Apollo 15 samples they studied, could not have supplied enough hydrogen to alter the D/H ratio of the most water-poor apatite. Their reasoning is further strengthened by the fact that all apatite analyzed in those samples had similarly low-δD values. However, in our study we observe that low-δD apatite is heterogeneous and is either directly affected by impact melt (secondary apatite) or is located inside a small clast (primary apatite) surrounded by impact melt, implying that they

most certainly experienced thermal processing. Furthermore, all primary low-δD apatites also show very complex nanostructures with sub-grain formation as a result of shock-deformation. Due to the textural context and the nanostructure of the low-δD apatite observed in our study, we conclude that networks of micro- to nanoscale grain boundaries could have acted as open pathways to enhance diffusion of hydrogen from D-poor regolith into the apatite grain, lowering its overall δD value, and resulting in its heterogeneous distribution. The regolith could have been either incorporated directly into the impact melt, or experienced thermal degassing caused by the heat of the impact melt, or both.

Unfortunately, we cannot estimate the amount of regolith that was assimilated in the impact melts, produced during large basin-forming impacts (e.g. Imbrium or Serenitatis), which are thought to be the likely sources of the breccias 72255 and 76255 (Thiessen et al., 2017). Although it is expected that the large basin-forming impacts would vaporize much of the regolith (e.g., Cintala, 1992), these breccias could have been formed as ejecta material further away from the impact crater where they incorporated or affected the local regolith. No further thermal processing of these samples had taken place after the impact event by which the breccias were formed. Furthermore, this study also reveals that the extent to which δD values can be affected during an impact largely depends on the initial water abundance of the host apatite. Regardless of the level of shock, only the water-poor apatite, exposed to shock deformation, appears to show extremely low-δD values. The apatites with extremely low-δD values are found within the same samples that also contain apatite with higher-δD values, with the overall microtextural setting strongly suggesting that they are of coeval origin, and thus unlikely to have sampled two separate δD reservoirs. On the other hand, apatite that contains more than ~ 100 ppm H_2O is unlikely to change its isotopic composition significantly, thus more likely to have preserved its primordial H isotopic composition.

5.3. Implications for source and timing of delivery of lunar water

Numerous petrogenetic models have been proposed to account for the contrasting primitive and evolved characteristics of the Mg-suite lithologies (summarized in Shearer et al., 2015). In brief, most models hypothesize partial melts of early LMO cumulates intruding into the overlying anorthositic crust, with a KREEP component either present in their source regions at the time of melting or being assimilated during their ascent. On the other hand, a few models have suggested involvement of large-scale (i.e., basin forming) impact events in producing at least a portion of the Mg-suite rocks (Shearer et al., 2015 and references therein), most recently of the troctolite 76535 (White et al., 2020). New research would be needed to understand the effect of the large-scale impact melting on volatile degassing of a large melt sheet and, consequently, on indigenous lunar volatile signature in cumulates crystalized within it. However, the impact-related models infer that the cumulates crystallized in insulated, slow-cooling large melt sheets or pooled beneath the anorthositic crust (summarized in Shearer et al., 2015), thus experiencing minimal degassing. Regardless of the exact mode of formation of Mg-suite rocks, their 'deep-seated' origin is universally accepted, suggesting that apatite crystallized in most of Mg-suite rocks would have experienced comparatively minimal, if any, H-isotope fractionation through degassing compared to those formed in mare basalts (e.g., Tartèse et al., 2014a,b). Thus most Mg-suite rocks are believed to directly record the primordial H isotopic composition of the lunar water (Barnes et al., 2016, 2014).

The lunar mantle derivatives seem to record variable δD values. The weighted average δD value of apatite in the Mg-suite obtained in this study ($-209 \pm 47‰$) coincides with the weighted aver-

age δD value estimated for lunar KREEPy samples (McCubbin and Barnes, 2019). In particular, the obtained δD value is similar to that of apatite in other plutonic rocks (Barnes et al., 2014), but also to that of basaltic lithologies in which apatite crystallized before any substantial degassing, such as in KREEP basalts (Tartèse et al., 2014a,b). Furthermore, it closely matches the values recently obtained for olivine-hosted melt inclusions in mare basalts (Singer et al., 2017). In contrast, anorthositic rocks (Hui et al., 2017; Greenwood et al., 2011) and olivine-hosted melt inclusions in volcanic glasses (Saal et al., 2013) record δD values of up to +350‰. Hui et al. (2017) attempted to explain the difference in the observed δD values between anorthosites and Mg-suite rocks by using a mixing model. However, the mixing model failed to reconcile the two different values and instead it was suggested that the two distinct sources could have originated from a layered LMO, in which surface anorthosites were affected by LMO degassing and, thus, recorded increased δD-values. The cumulates in the lower portion of the LMO, such as Mg-suite rocks, sample primordial δD that was largely unaffected by magmatic degassing. The δD value obtained in the current study (−209 ± 47‰), indistinguishable from other KREEPy lunar rocks (McCubbin and Barnes, 2019), suggests that early lunar mantle, or deeper layers of LMO, have δD strikingly similar to terrestrial deep mantle (Hallis et al., 2015). This further strengthens the existing hypothesis of a common origin of water on Earth and Moon.

Based on recent FTIR measurements in ferroan anorthosite plagioclase (Hui et al., 2013, 2017) and some other studies (Chen et al., 2015; McCubbin et al., 2015) it has been estimated that the LMO contained ∼136 ppm of water. Models suggest that this amount of water was likely to be too high to survive the Moon-forming impact (Elkins-Tanton and Grove, 2011). Instead, most of the water in lunar interior was suggested to have accumulated during the protracted evolution of the LMO sometime between 10 and 200 Ma after the formation of the Moon (Tartèse and Anand, 2013 and references therein), with only up to 25% of terrestrial water contributing towards the entire lunar budget (Barnes et al., 2016). In a recent study, Greenwood et al. (2018) suggested that most of the terrestrial water was formed during planetary accretion, before the Moon-forming impact occurred. They further set the constraints on composition of the Late Veneer based on the oxygen isotopes, that most likely CM and water-poor enstatite chondrites delivered water to the Earth. On the other hand, the composition of the Late Veneer determined by the water abundance in lunar samples concluded that other types of carbonaceous chondrites in addition to CM – CO, CI, and possibly CV – acted as a source of water (Barnes et al., 2016). The similarities in the mantle values of terrestrial and lunar water, followed by the assumption that most of terrestrial water was delivered before Moon formed, dictate that the chondrites accreted on Earth prior to the Giant Impact must have been of comparable composition to those accreted on both planets during the Late Veneer, and, thus, during the time when most of Mg-suite apatite crystallized (10–200 Ma after the Giant Impact). Furthermore, the current study reveals that the H isotopic composition of apatites within the early lunar crustal rocks (≥4.2 Ga; 76335; 78235; 78236) and impact-melt breccias formed at ∼3.9 Ga (72255, 73235 and 76255) are similar. Based on this fact, it can be hypothesized that throughout the early bombardment history of the Moon, impactors delivered water of the composition similar to indigenous lunar and terrestrial water (i.e., impactors did not vary in composition significantly, at least in their H isotopic composition; e.g., CM, CO, CI, and possibly CV) or that they had low water abundances (e.g., enstatite chondrites) and hence no capacity to affect the H isotopic composition of pre-existing water in the primary lunar rocks.

6. Conclusions

This study reports on the chemistry, water abundance and H isotopic composition of Mg-suite apatite from troctolite, gabbro and norite lithologies that show variable degrees of shock-deformation. Petrographic context, microtextural and nanostructural inspection reveal two distinct types of apatite: primary (with shock stages S1–S6) and secondary (recrystallized or grown from impact melt). No obvious difference in mineral composition, H_2O abundance and δD was observed between the two textural types. Mg-suite apatite studied here contains up to ∼960 ppm of H_2O and shows δD values (−535 ± 134‰ to +147 ± 194‰) within the range of terrestrial and carbonaceous chondrite values, with the weighted average δD values of −209 ± 47‰ being indistinguishable from the Earth's deeper mantle. H_2O-δD systematics of apatite do not correlate with the level of shock each apatite grain has experienced, but it is apparent that individual water-poor apatite grains were influenced by a process, which resulted in the lowering of their original δD values. The grains with the lowest δD values are either in contact with impact melt or have severely complex nanostructures induced by shock-deformation. Locally, on a level of an individual grain, the network of grain boundaries could enhance reaction with D-poor regolith, which is thermally processed by a hot impact-melt, resulting in D-poor signature of apatite. Water-rich primary apatites (above ∼100 ppm H_2O) that contain complex microtextures do not show any evidence of significant water-loss or alteration in their δD value. Thus, water-rich apatites in some of the oldest lunar crustal materials act as a reliable recorder of the primordial H isotopic signature of the Moon, despite experiencing variable degrees of shock-deformation at a later stage in lunar history.

Authors contributions

AC, MA: Study design, Methodology, MA: Supervision, AC, JRD, LFW, XC, and IAF: Formal analyzes, AC, AS, XC, IAF, JRD, LFW: Data reduction and processing, AC: Writing – Original draft preparation, All authors: Draft reviewing and editing.

Declaration of competing interest

The authors declare that they have no known competing financial interests or personal relationships that could have appeared to influence the work reported in this paper.

Acknowledgements

Appendix A. Supplementary material

Supplementary material related to this article can be found online at https://doi.org/10.1016/j.epsl.2020.116364.

References

Adcock, C.T., Tschauner, O., Hausrath, E.M., Udry, A., Luo, S.N., Cai, Y., Ren, M., Lanzirotti, A., Newville, M., Kunz, M., Lin, C., 2017. Shock-transformation of whit-

lockite to merrillite and the implications for meteoritic phosphate. Nat. Commun. 8, 14667. https://doi.org/10.1038/ncomms14667.

Alexander, Conel M.O'D., 2017. The origin of inner Solar System water. Philos. Trans. - Royal Soc., Math. Phys. Eng. Sci. 375, 20150384. https://doi.org/10.1098/rsta.2015.0384.

Alexander, C.M.O., Bowden, R., Fogel, M.L., Howard, K.T., Herd, C.D.K., Nittler, L.R., 2012. The provenances of asteroids, and their contributions to the volatile inventories of the terrestrial planets. Science 337, 721–723. https://doi.org/10.1126/science.1223474.

Anand, M., 2014. Analyzing Moon rocks. Science 344, 365–366. https://doi.org/10.1126/science.1253266.

Barnes, J.J., Franchi, I.A., Anand, M., Tartèse, R., Starkey, N.A., Koike, M., Sano, Y., Russell, S.S., 2013. Accurate and precise measurements of the D/H ratio and hydroxyl content in lunar apatites using NanoSIMS. Chem. Geol. 337–338, 48–55. https://doi.org/10.1016/j.chemgeo.2012.11.015.

Barnes, J.J., Tartèse, R., Anand, M., McCubbin, F.M., Franchi, I.A., Starkey, N.A., Russell, S.S., 2014. The origin of water in the primitive Moon as revealed by the lunar highlands samples. Earth Planet. Sci. Lett. 390, 244–252. https://doi.org/10.1016/j.epsl.2014.01.015.

Barnes, J.J., Tartèse, R., Anand, M., McCubbin, F.M., Neal, C.R., Franchi, I.A., 2016. Early degassing of lunar urKREEP by crust-breaching impact(s). Earth Planet. Sci. Lett. 447, 84–94. https://doi.org/10.1016/j.epsl.2016.04.036.

Barrett, T.J., Barnes, J.J., Tartèse, R., Anand, M., Franchi, I.A., Greenwood, R.C., Charlier, B.L.A., Grady, M.M., 2016. The abundance and isotopic composition of water in eucrites. Meteorit. Planet. Sci. 51, 1110–1124. https://doi.org/10.1111/maps.12649.

Bogard, D.D., Nyquist, L.E., Hirsch, W.C., 1975. Noble gases in Apollo 17 boulders and soils. In: Lunar and Planetary Science Conference, vol. 5, p. 73.

Boyce, J.W., Liu, Y., Rossman, G.R., Guan, Y., Eiler, J.M., Stolper, E.M., Taylor, L.A., 2010. Lunar apatite with terrestrial volatile abundances. Nature 466, 466–469. https://doi.org/10.1038/nature09274.

Boyce, J.W., Tomlinson, S.M., McCubbin, F.M., Greenwood, J.P., Treiman, A.H., 2014. The lunar apatite paradox. Science 344, 400–402. https://doi.org/10.1126/science.1250398.

Chen, Y., Zhang, Y., Liu, Y., Guan, Y., Eiler, J., Stolper, E.M., 2015. Water, fluorine, and sulfur concentrations in the lunar mantle. Earth Planet. Sci. Lett. 427, 37–46. https://doi.org/10.1016/j.epsl.2015.06.046.

Cintala, M.J., 1992. Impact-induced thermal effects in the lunar and Mercurian regoliths. J. Geophys. Res., Planets 97, 947–973. https://doi.org/10.1029/91JE02207.

Černok, A., White, L.F., Darling, J., Dunlop, J., Anand, M., 2019. Shock-induced microtextures in lunar apatite and merrillite. Meteorit. Planet. Sci. 54, 1262–1282. https://doi.org/10.1111/maps.13278.

Darling, J.R., Moser, D.E., Barker, I.R., Tait, K.T., Chamberlain, K.R., Schmitt, A.K., Hyde, B.C., 2016. Variable microstructural response of baddeleyite to shock metamorphism in young basaltic shergottite NWA 5298 and improved U-Pb dating of Solar System events. Earth Planet. Sci. Lett. 444, 1–12. https://doi.org/10.1016/j.epsl.2016.03.032.

Elkins-Tanton, L.T., Grove, T.L., 2011. Water (hydrogen) in the lunar mantle: results from petrology and magma ocean modeling. Earth Planet. Sci. Lett. 307, 173–179. https://doi.org/10.1016/j.epsl.2011.04.027.

Füri, E., Deloule, E., Gurenko, A., Marty, B., 2014. New evidence for chondritic lunar water from combined D/H and noble gas analyses of single Apollo 17 volcanic glasses. Icarus 229, 109–120. https://doi.org/10.1016/j.icarus.2013.10.029.

Füri, E., Deloule, E., Trappitsch, R., 2017. The production rate of cosmogenic deuterium at the Moon's surface. Earth Planet. Sci. Lett. 474, 76–82. https://doi.org/10.1016/j.epsl.2017.05.042.

Göpel, C., Manhès, G., Allègre, C.J., 1994. U-Pb systematics of phosphates from equilibrated ordinary chondrites. Earth Planet. Sci. Lett. 121, 153–171. https://doi.org/10.1016/0012-821X(94)90038-8.

Greenwood, J.P., Itoh, S., Sakamoto, N., Warren, P., Taylor, L., Yurimoto, H., 2011. Hydrogen isotope ratios in lunar rocks indicate delivery of cometary water to the Moon. Nat. Geosci. 4, 79–82. https://doi.org/10.1038/ngeo1050.

Greenwood, R.C., Barrat, J.-A., Miller, M.F., Anand, M., Dauphas, N., Franchi, I.A., Sillard, P., Starkey, N.A., 2018. Oxygen isotopic evidence for accretion of Earth's water before a high-energy Moon-forming giant impact. Sci. Adv. 4, eaao5928. https://doi.org/10.1126/sciadv.aao5928.

Hallis, L.J., 2017. D/H ratios of the inner Solar System. Philos. Trans. R. Soc., Math. Phys. Eng. Sci. 375, 20150390. https://doi.org/10.1098/rsta.2015.0390.

Hallis, L.J., Huss, G.R., Nagashima, K., Taylor, G.J., Halldórsson, S.A., Hilton, D.R., Mottl, M.J., Meech, K.J., 2015. Evidence for primordial water in Earth's deep mantle. Science 350, 795–797. https://doi.org/10.1126/science.aac4834.

Hallis, L.J., Huss, G.R., Nagashima, K., Taylor, G.J., Stöffler, D., Smith, C.L., Lee, M.R., 2017. Effects of shock and Martian alteration on Tissint hydrogen isotope ratios and water content. Geochim. Cosmochim. Acta 200, 280–294. https://doi.org/10.1016/j.gca.2016.12.035.

Hauri, E.H., Weinreich, T., Saal, A.E., Rutherford, M.C., Orman, J.A.V., 2011. High pre-eruptive water contents preserved in Lunar melt inclusions. Science 333, 213–215. https://doi.org/10.1126/science.1204626.

Higashi, Y., Itoh, S., Hashiguchi, M., Sakata, S., Hirata, T., Watanabe, K., Sakaguchi, I., 2017. Hydrogen diffusion in the apatite-water system: fluorapatite parallel to the c-axis. Geochem. J. 51, 115–122. https://doi.org/10.2343/geochemj.2.0460.

Howarth, G.H., Pernet-Fisher, J.F., Bodnar, R.J., Taylor, L.A., 2015. Evidence for the exsolution of Cl-rich fluids in martian magmas: apatite petrogenesis in the enriched lherzolitic shergottite Northwest Africa 7755. Geochim. Cosmochim. Acta 166, 234. https://doi.org/10.1016/j.gca.2015.06.031.

Hughes, J.M., 2015. The many facets of apatite. Am. Mineral. 100, 1033–1039. https://doi.org/10.2138/am-2015-5193.

Hui, H., Guan, Y., Chen, Y., Peslier, A.H., Zhang, Y., Liu, Y., Flemming, R.L., Rossman, G.R., Eiler, J.M., Neal, C.R., Osinski, G.R., 2017. A heterogeneous lunar interior for hydrogen isotopes as revealed by the lunar highlands samples. Earth Planet. Sci. Lett. 473, 14–23. https://doi.org/10.1016/j.epsl.2017.05.029.

Hui, H., Peslier, A.H., Zhang, Y., Neal, C.R., 2013. Water in lunar anorthosites and evidence for a wet early Moon. Nat. Geosci. 6, 177–180. https://doi.org/10.1038/ngeo1735.

Johnson, E.A., Rossman, G.R., 2013. The diffusion behavior of hydrogen in plagioclase feldspar at 800–1000°C: implications for re-equilibration of hydroxyl in volcanic phenocrysts. Am. Mineral. 98, 1779–1787. https://doi.org/10.2138/am.2013.4521.

Kenny, G.G., Karlsson, A., Schmieder, M., Whitehouse, M.J., Nemchin, A.A., Bellucci, J.J., 2020. Recrystallization and chemical changes in apatite in response to hypervelocity impact. Geology 48, 19–23. https://doi.org/10.1130/G46575.1.

Konecke, B.A., Fiege, A., Simon, A.C., Parat, F., Stechern, A., 2017. Co-variability of S6+, S4+, and S2− in apatite as a function of oxidation state: implications for a new oxybarometer. Am. Mineral. 102, 548–557. https://doi.org/10.2138/am-2017-5907.

Leich, D.A., Kahl, S.B., Kirschbaum, A.R., Niemeyer, S., Phinney, D., 1975. Rare Gas Constraints on the History of Boulder 1, Station 2, Apollo 17, Moon 14, p. 407.

Liu, Y., Guan, Y., Zhang, Y., Rossman, G.R., Eiler, J.M., Taylor, L.A., 2012. Direct measurement of hydroxyl in the lunar regolith and the origin of lunar surface water. Nat. Geosci. 5, 779–782. https://doi.org/10.1038/ngeo1601.

McCubbin, F.M., Barnes, J.J., 2019. Origin and abundances of H₂O in the terrestrial planets, Moon, and asteroids. Earth Planet. Sci. Lett. 526, 115771. https://doi.org/10.1016/j.epsl.2019.115771.

McCubbin, F.M., Hauri, E.H., Elardo, S.M., Kaaden, K.E.V., Wang, J., Shearer, C.K., 2012. Hydrous melting of the martian mantle produced both depleted and enriched shergottites. Geology, G33242.1. https://doi.org/10.1130/G33242.1.

McCubbin, F.M., Jones, R.H., 2015. Extraterrestrial apatite: planetary geochemistry to astrobiology. Elements 11, 183–188. https://doi.org/10.2113/gselements.11.3.183.

McCubbin, F.M., Steele, A., Hauri, E.H., Nekvasil, H., Yamashita, S., Hemley, R.J., 2010. Nominally hydrous magmatism on the Moon. Proc. Natl. Acad. Sci. 107, 11223–11228. https://doi.org/10.1073/pnas.1006677107.

McCubbin, F.M., Kaaden, K.E.V., Tartèse, R., Klima, R.L., Liu, Y., Mortimer, J., Barnes, J.J., Shearer, C.K., Treiman, A.H., Lawrence, D.J., Elardo, S.M., Hurley, D.M., Boyce, J.W., Anand, M., 2015. Magmatic volatiles (H, C, N, F, S, Cl) in the lunar mantle, crust, and regolith: abundances, distributions, processes, and reservoirs. Am. Mineral. 100, 1668–1707. https://doi.org/10.2138/am-2015-4934CCBYNCND.

Merlivat, L., Lelu, M., Nief, G., Roth, E., 1976. Spallation deuterium in rock 70215. In: Proc. 7th Lunar Planet. Sci. Conf, pp. 649–658.

Minitti, M.E., Leshin, L.A., Dyar, M.D., Ahrens, T.J., Guan, Y., Luo, S.-N., 2008a. Assessment of shock effects on amphibole water contents and hydrogen isotope compositions, 2: kaersutitic amphibole experiments. Earth Planet. Sci. Lett. 266, 288–302. https://doi.org/10.1016/j.epsl.2007.11.012.

Minitti, M.E., Rutherford, M.J., Taylor, B.E., Dyar, M.D., Schultz, P.H., 2008b. Assessment of shock effects on amphibole water contents and hydrogen isotope compositions, 1: amphibolite experiments. Earth Planet. Sci. Lett. 266, 46–60. https://doi.org/10.1016/j.epsl.2007.10.047.

Ni, P., Zhang, Y., Chen, S., Gagnon, J., 2019. A melt inclusion study on volatile abundances in the lunar mantle. Geochim. Cosmochim. Acta 249, 17–41. https://doi.org/10.1016/j.gca.2018.12.034.

Ni, P., Zhang, Y., Guan, Y., 2017. Volatile loss during homogenization of lunar melt inclusions. Earth Planet. Sci. Lett. 478, 214–224. https://doi.org/10.1016/j.epsl.2017.09.010.

Pernet-Fisher, J.F., Howarth, G.H., Liu, Y., Chen, Y., Taylor, L.A., 2014. Estimating the lunar mantle water budget from phosphates: complications associated with silicate-liquid-immiscibility. Geochim. Cosmochim. Acta 144, 326–341. https://doi.org/10.1016/j.gca.2014.09.004.

Robinson, K.L., Barnes, J.J., Nagashima, K., Thomen, A., Franchi, I.A., Huss, G.R., Anand, M., Taylor, G.J., 2016. Water in evolved lunar rocks: evidence for multiple reservoirs. Geochim. Cosmochim. Acta 188, 244–260. https://doi.org/10.1016/j.gca.2016.05.030.

Robinson, K.L., Taylor, G.J., 2014. Heterogeneous distribution of water in the Moon. Nat. Geosci. 7, 401–408. https://doi.org/10.1038/ngeo2173.

Saal, A.E., Hauri, E.H., Cascio, M.L., Van Orman, J.A., Rutherford, M.C., Cooper, R.F., 2008. Volatile content of lunar volcanic glasses and the presence of water in the Moon's interior. Nature 454, 192–195. https://doi.org/10.1038/nature07047.

Saal, A.E., Hauri, E.H., Orman, J.A.V., Rutherford, M.J., 2013. Hydrogen isotopes in lunar volcanic glasses and melt inclusions reveal a carbonaceous chondrite heritage. Science 340, 1317–1320. https://doi.org/10.1126/science.1235142.

Shearer, C.K., Elardo, S.M., Petro, N.E., Borg, L.E., McCubbin, F.M., 2015. Origin of the lunar highlands Mg-suite: an integrated petrology, geochemistry, chronology, and remote sensing perspective. Am. Mineral. 100, 294–325. https://doi.org/10.2138/am-2015-4817.

Singer, J.A., Greenwood, J.P., Itoh, S., Sakamoto, N., Yurimoto, H., 2017. Evidence for the solar wind in lunar magmas: a study of slowly cooled samples of the Apollo 12 olivine basalt suite. Geochem. J. 51, 95–104. https://doi.org/10.2343/geochemj.2.0462.

Stephant, A., Robert, F., 2014. The negligible chondritic contribution in the lunar soils water. Proc. Natl. Acad. Sci. 111, 15007–15012. https://doi.org/10.1073/pnas.1408118111.

Tartèse, R., Anand, M., 2013. Late delivery of chondritic hydrogen into the lunar mantle: insights from mare basalts. Earth Planet. Sci. Lett. 361, 480–486. https://doi.org/10.1016/j.epsl.2012.11.015.

Tartèse, R., Anand, M., Barnes, J.J., Starkey, N.A., Franchi, I.A., Sano, Y., 2013. The abundance, distribution, and isotopic composition of Hydrogen in the Moon as revealed by basaltic lunar samples: implications for the volatile inventory of the Moon. Geochim. Cosmochim. Acta 122, 58–74. https://doi.org/10.1016/j.gca.2013.08.014.

Tartèse, R., Anand, M., Joy, K.H., Franchi, I.A., 2014a. H and Cl isotope systematics of apatite in brecciated lunar meteorites Northwest Africa 4472, Northwest Africa 773, Sayh al Uhaymir 169, and Kalahari 009. Meteorit. Planet. Sci. 49, 2266–2289. https://doi.org/10.1111/maps.12398.

Tartèse, R., Anand, M., McCubbin, F.M., Elardo, S.M., Shearer, C.K., Franchi, I.A., 2014b. Apatites in lunar KREEP basalts: the missing link to understanding the H isotope

systematics of the Moon. Geology 42, 363–366. https://doi.org/10.1130/G35288.1.

Taylor, L.A., Patchen, A., Mayne, R.G., Taylor, D.-H., 2004. The most reduced rock from the moon, Apollo 14 basalt 14053: its unique features and their origin. Am. Mineral. 89, 1617–1624. https://doi.org/10.2138/am-2004-11-1205.

Thiessen, F., Nemchin, A.A., Snape, J.F., Whitehouse, M.J., Bellucci, J.J., 2017. Impact history of the Apollo 17 landing site revealed by U-Pb SIMS ages. Meteorit. Planet. Sci. 52, 584–611. https://doi.org/10.1111/maps.12814.

Treiman, A.H., Boyce, J.W., Greenwood, J.P., Eiler, J.M., Gross, J., Guan, Y., Ma, C., Stolper, E.M., 2016. D-poor hydrogen in lunar mare basalts assimilated from lunar regolith. Am. Mineral. 101, 1596–1603. https://doi.org/10.2138/am-2016-5582.

Warren, P.H., 1993. A consise compilation of petrologic information on possibly pristine nonmare Moon rocks. Am. Mineral. 78, 360–376.

White, L.F., Černok, A., Darling, J.R., Whitehouse, M.J., Joy, K.H., Cayron, C., Dunlop, J., Tait, K.T., Anand, M., 2020. Evidence of extensive lunar crust formation in impact melt sheets 4,330 Myr ago. Nat. Astron., 1–5. https://doi.org/10.1038/s41550-020-1092-5.